NASA/TM-20230015316

Tail-Cone Thruster Fan Rotor Flutter Analysis

Akiva R. Wernick
HX5, LLC, Brook Park, Ohio

Milind A. Bakhle
Glenn Research Center, Cleveland, Ohio

December 2023

NASA STI Program . . . in Profile

Since its founding, NASA has been dedicated to the advancement of aeronautics and space science. The NASA Scientific and Technical Information (STI) Program plays a key part in helping NASA maintain this important role.

The NASA STI Program operates under the auspices of the Agency Chief Information Officer. It collects, organizes, provides for archiving, and disseminates NASA's STI. The NASA STI Program provides access to the NASA Technical Report Server—Registered (NTRS Reg) and NASA Technical Report Server—Public (NTRS) thus providing one of the largest collections of aeronautical and space science STI in the world. Results are published in both non-NASA channels and by NASA in the NASA STI Report Series, which includes the following report types:

- TECHNICAL PUBLICATION. Reports of completed research or a major significant phase of research that present the results of NASA programs and include extensive data or theoretical analysis. Includes compilations of significant scientific and technical data and information deemed to be of continuing reference value. NASA counter-part of peer-reviewed formal professional papers, but has less stringent limitations on manuscript length and extent of graphic presentations.

- TECHNICAL MEMORANDUM. Scientific and technical findings that are preliminary or of specialized interest, e.g., "quick-release" reports, working papers, and bibliographies that contain minimal annotation. Does not contain extensive analysis.

- CONTRACTOR REPORT. Scientific and technical findings by NASA-sponsored contractors and grantees.

- CONFERENCE PUBLICATION. Collected papers from scientific and technical conferences, symposia, seminars, or other meetings sponsored or co-sponsored by NASA.

- SPECIAL PUBLICATION. Scientific, technical, or historical information from NASA programs, projects, and missions, often concerned with subjects having substantial public interest.

- TECHNICAL TRANSLATION. English-language translations of foreign scientific and technical material pertinent to NASA's mission.

For more information about the NASA STI program, see the following:

- Access the NASA STI program home page at http://www.sti.nasa.gov

- E-mail your question to help@sti.nasa.gov

- Fax your question to the NASA STI Information Desk at 757-864-6500

- Telephone the NASA STI Information Desk at 757-864-9658

- Write to:
  NASA STI Program
  Mail Stop 148
  NASA Langley Research Center
  Hampton, VA 23681-2199

NASA/TM-20230015316

Tail-Cone Thruster Fan Rotor Flutter Analysis

Akiva R. Wernick
HX5, LLC, Brook Park, Ohio

Milind A. Bakhle
Glenn Research Center, Cleveland, Ohio

National Aeronautics and
Space Administration

Glenn Research Center
Cleveland, Ohio 44135

December 2023

Acknowledgments

The authors would like to gratefully acknowledge the support received from other researchers. Thank you to Timothy Beach for creating the computational mesh, Wai-Ming To and Gregory Heinlein for the TURBO stage analyses, James Min for Ansys finite-element method analyses, Austin Schemmel for mapping mode shapes, Rula Coroneos for related Nastran structural analyses, Kristopher Pierson for providing suggestions to improve this report and for sharing findings from his related work, Jen-Ping Chen (The Ohio State University) for sharing his input with regard to this work and for his help in connecting the authors of this work together, and Paul Giel for facilitating this work and report. The authors gratefully acknowledge the support of this work provided by the NASA Advanced Air Transport Technology Project and the Transformational Tools and Technologies Project. Computational resources supporting this work were provided by the NASA High-End Computing (HEC) Program through the NASA Advanced Supercomputing (NAS) Division at Ames Research Center.

This work was sponsored by the Advanced Air Vehicles Program
at the NASA Glenn Research Center.

Level of Review: This material has been technically reviewed by technical management.

This report is available in electronic form at https://www.sti.nasa.gov/ and https://ntrs.nasa.gov/

Tail-Cone Thruster Fan Rotor Flutter Analysis

Akiva R. Wernick*
HX5, LLC
Brook Park, Ohio 44142

Milind A. Bakhle
National Aeronautics and Space Administration
Glenn Research Center
Cleveland, Ohio 44135

Summary

The aeroelastic stability of a tail-cone thruster fan was analyzed for three structural modes and various nodal diameter patterns. Computational fluid dynamics modeling with blade vibrations was used in the analyses performed at design (peak-efficiency) condition and two near-stall conditions at the design rotational speed. Aerodynamic damping (aerodamping) was used to assess flutter because this integrally bladed rotor design will have minimal structural damping. Aerodamping was found to be low at the design condition. For the first mode, aerodamping was seen to decrease toward stall, vanishing for a zero nodal diameter pattern. Further decrease in mass flow led to negative aerodamping (flutter) for the first and second nodal diameters in the near-stall condition. The flow field at this lowest mass flow rate exhibited some additional unsteadiness at higher frequency. The sensitivity of results to time step and amplitudes of vibration was examined and found to be very satisfactory. The largest uncertainty in the results comes from the observed sensitivity of the aerodamping to details of the variations in grid deformations in the blade passage mesh from the blade to the boundaries. For the parametric variations analyzed, the calculated aerodamping is lower if the grid deformations near the blade surface are higher. Further work is needed to understand the cause of this sensitivity and find possible solutions to reduce the effects on flutter predictions.

1.0 Introduction

NASA has introduced new goals for the noise, emissions, and performance of future-generation aircraft with entry into service in the years 2030 to 2035 (Ref. 1). One approach to achieving these goals is the use of boundary-layer ingestion (BLI) propulsion with engine inlets that would be located on the upper surface near the tail end of the aircraft (Refs. 2 to 5). BLI engines are designed to utilize slow-moving flow that would otherwise form the wake of the aircraft and act as drag. This design reduces the overall loss associated with the aircraft (Ref. 2).

Fans operating in a BLI engine experience unsteady loadings due to the distortion field produced by the ingested boundary layer. The unsteady loadings acting on the rotors can yield forced vibrational responses, resulting in vibrational stresses (Ref. 4). In the design process of a BLI fan, it is necessary to verify that the fan blades can withstand the vibration response and dynamic stresses resulting from aerodynamic excitation of various structural modes that will occur at different operating and flight conditions. Previous research efforts examined the vibrational effects the distortion field has on a distortion-tolerant fan rotor used in a BLI fan (Refs. 4 and 5). That work used numerical modeling to

*Currently with Cornerstone Research Group.

examine the vibrational modes of the fan rotor and the flutter stability of these modes at select operating conditions.

This report applies the concepts described in References 4 and 5 to a tail-cone thruster (TCT) fan designed for a BLI propulsion system. At the design rotational speed, the aeroelastic stability of three structural modes was examined for various nodal diameter patterns. The vibrational mode shapes and frequencies of the rotor were computed using a commercial finite element method (FEM) analysis code. Blade mode shapes were then provided as an input to a computational fluid dynamics (CFD) model to compute the aerodynamic damping, or aerodamping, using the energy method (Ref. 6) as the ratio of the work per cycle and kinetic energy for each mode shape and nodal diameter. Aerodamping is expressed as a (viscous) damping ratio of actual to critical damping, often represented by ζ.

2.0 Numerical Model

The CFD model used in the present work is a 3D numerical solver called TURBO, which is designed for turbomachinery and solves the unsteady Reynolds-averaged Navier–Stokes equations. In previous work, this solver has also been referred to as TURBO–AE. The current version incorporates the relevant feature of vibrating blades to evaluate aerodamping for flutter. TURBO utilizes an implicit finite-volume code for structured multiple-block grids (Ref. 5). A decoupled k–ε model, where k is turbulent kinetic energy and ε is its rate of dissipation, is used for TURBO's turbulence modeling. TURBO is capable of modeling nonlinear flow features and relative interactions between nonvibrating blades (Ref. 7). TURBO has the capability to model the interaction effects of vibrating blades and the surrounding flow fields. TURBO calculates the work per cycle for each blade or for the full rotor, which can be converted into an aerodamping value for flutter analysis.

The mesh or grid deformations used in TURBO's aeroelastic analysis are based on blade mode shapes (modal displacements) from experimental measurements or computational structural modeling that are then propagated through the entire CFD mesh. For the energy method, TURBO does not use two-way coupling, which means the harmonic blade vibration amplitudes are predetermined and prescribed in the simulation. TURBO takes in the complex-valued mesh deformation amplitudes for a selected mode shape and nodal diameter as input and applies a harmonic time function to deform the original mesh at each time step to simulate a traveling wave vibration. The user-specified vibrational frequency in the time function is typically the natural frequency. The deformation input files, based on modal deformations, are scaled in TURBO using a user-specified scaling factor. In this report, the scaling factor is also referred to as the "amplitude."

For this study, the fan rotor being analyzed is a 16-blade configuration. Each blade passage is modeled using an O-mesh surrounding the blade airfoil and H-meshes for the other parts of the passage. The surface deformations were computed using the commercially available Ansys Mechanical™ (ANSYS, Inc.) FEM modeling and analysis tool, which calculated the mode shapes for the first three modes and all nodal diameters. The modal displacements for each nodal diameter were very similar, so only a single mode shape (from each mode family) was used to model the vibrational effects in TURBO. As is typical, the 8-nodal-diameter (8ND) mode shape (corresponding to half the blade count) from the FEM analysis was selected because it represents the typical blade-alone vibration characteristics rather than those of any particular nodal diameter vibration pattern with blade-disk coupling. For this configuration, the natural frequencies in the first three mode families varied only slightly with nodal diameter. The grid deformation input files for TURBO were generated using a stand-alone special-purpose preprocessor code developed as part of this study. This code propagates the grid deformations from the blade surface into the blade passage using an exponential decay function such that the

deformations are zero at the outer bounds of the mesh (the blade passage boundaries). The external code allows the user to specify the rate at which the deformations decrease from the blade surface by controlling the coefficient in the exponent of the exponential function; this coefficient will be referred to as the "decay coefficient." Details of the mesh deformation algorithm and implementation are described in the following section.

3.0 Mesh Deformation

The deformation file input for TURBO is generated using an external code designed specifically for blades with an O-mesh configuration. The algorithm first reads in an input file containing the deformations associated with the blade surface along with the PLOT3D-formatted mesh files associated with the blade. The algorithm then begins by assigning a parameter value, P, defined by Equation (1) at an approximately constant spanwise location in the passage such that the parameter has a value of 0 on the blade surface and increases outward from the blade surface to the blade passage boundary, where the value is 1.

$$P = \frac{d_{bld}}{d_{bld} + d_{bnd}} \tag{1}$$

where d_{bld} is the distance from the blade surface and d_{bnd} is the distance from the bounds of the mesh. The deformations at each node of the mesh are then computed using the exponential decay function defined in Equation (2), which ensures that the deformations at the blade surface are equal to the inputted surface deformation data and that the deformations at the bounds of the mesh are zero.

$$\Delta x(P) = \frac{e^{-\lambda P} - e^{-\lambda P_{bnd}}}{e^{-\lambda P_{bld}} - e^{-\lambda P_{bnd}}} \Delta x_{bld} \tag{2a}$$

or

$$\Delta x(P) = \frac{e^{-\lambda P} - e^{-\lambda}}{1 - e^{-\lambda}} \Delta x_{bld} \tag{2b}$$

where Δx represents the deformation components. Equations (2), (3), (4), and (6) show how Δx is calculated; similar calculations would be used for calculating Δy and Δz. The parameter λ is the decay coefficient associated with the exponential decay function.

A modification to the algorithm is used to handle the mesh in the tip gap region between the blade tip and the casing or shroud. First, the deformations are propagated through the blocks associated with the tip gap region before being propagated through the rest of the mesh. The tip gap region is assigned a parameter value ranging from 0 to 1, similar to the approach shown in Equation (1) except that the bounds of the mesh are only associated with the casing within the tip gap region. The deformations on the outer edge of the tip gap region are first computed using a linear interpolation shown in Equation (3) such that the casing has 0 deformations.

$$\Delta x(P) = \Delta x_{bld} \left(1 - \frac{P - P_{bld}}{P_{cas} - P_{bld}} \right) \tag{3a}$$

where the subscript *cas* refers to the values at the casing and the other variables are analogous to the variables described in Equations (1) and (2). Because $P_{cas} = 1$ and $P_{bld} = 0$, Equation (3a) simplifies to

$$\Delta x(P) = \Delta x_{bld}\,(1 - P) \tag{3b}$$

Next, the deformations within the tip gap region are computed as a weighted average of the deformations on the outer edge of the region and weighted by the reciprocal of the distance from the point in question to the edge of the tip gap region.

$$\Delta x_p = \frac{\sum_{n=1}^{n_{\text{edge}}} \frac{\Delta x_n}{d_n}}{\sum_{n=1}^{n_{\text{edge}}} \frac{1}{d_n}} \tag{4}$$

where n_{edge} is the number of points that lie on the edge of the tip gap region, n is the index associated with a point on the edge, and d is the distance from the point p to the point n that lies on the edge. The algorithm then treats the edge of the tip gap region as an extension of the blade and uses the method described above to fill in the deformations within the rest of the mesh.

The algorithm is performed on a single blade passage and is rotated to form the full annulus using Equations (5a) to (5c) for the respective x, y, and z components of the deformations. The phasing is then applied to the deformations in each blade passage using Equations (6a) and (6b) to compute the real and imaginary components of the deformations. Note that the x-axis is the axis of fan rotation and symmetry.

$$\Delta x = \Delta x_{b=1} \tag{5a}$$

$$\Delta y = \Delta z_{b=1} \sin\left[(b-1)\theta\right] + \Delta y_{b=1} \cos\left[(b-1)\theta\right] \tag{5b}$$

$$\Delta z = \Delta z_{b=1} \cos\left[(b-1)\theta\right] - \Delta y_{b=1} \sin\left[(b-1)\theta\right] \tag{5c}$$

where b refers to the current blade passage within the full annulus, the subscript $b = 1$ refers to the blade passage used to compute the initial deformations through the mesh, and θ refers to the angle between blade passages (pitch angle), which for the TCT geometry is 22.5° for the 16-blade passage configuration.

$$\Delta x_r = \Delta x \sin\left[(b-1)\varphi\right] \tag{6a}$$

$$\Delta x_i = \Delta x \cos\left[(b-1)\varphi\right] \tag{6b}$$

where the subscripts r and i refer to the real and imaginary components of Δx, and φ refers to the interblade phase angle.

Figure 1 illustrates the structural mode shapes mapped on the blade surface. The contours of deformation magnitude shown in Figure 1 are for mode shapes that are normalized to unit mass. A scaling factor is applied to the deformations when read into TURBO to limit the maximum grid deformations in the simulation. Figure 2 visualizes how the deformations propagate through the mesh using a decay coefficient of 1 in the exponential decay function (for mode 1).

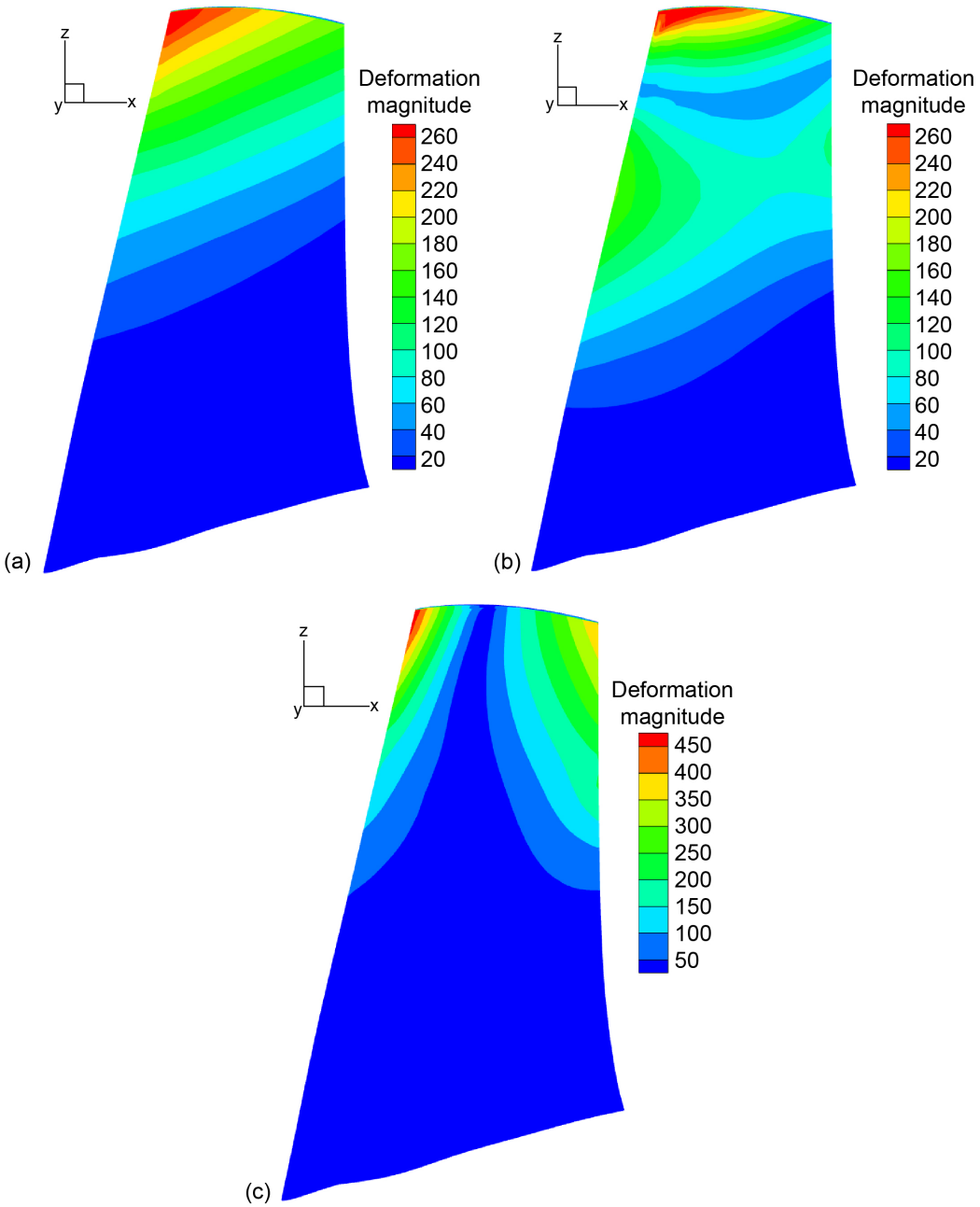

Figure 1.—TCT deformations. (a) Mode 1. (b) Mode 2. (c) Mode 3.

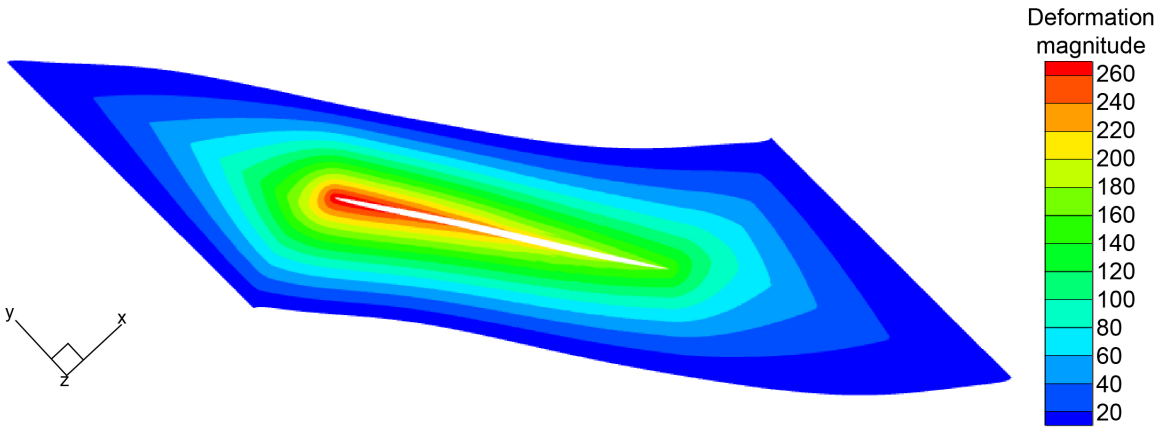

Figure 2.—TCT mode 1 deformation propagation at constant radius.

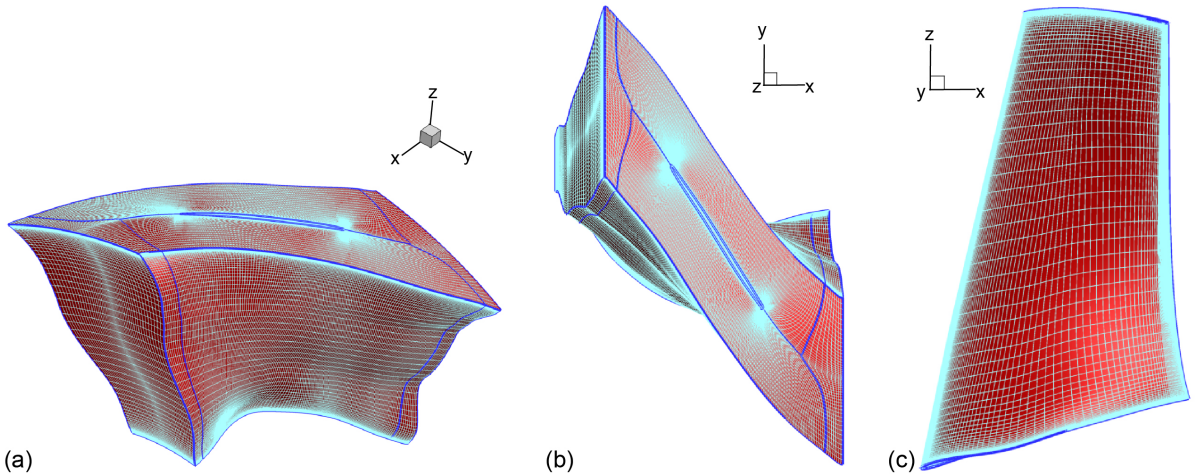

Figure 3.—TCT single-passage mesh. (a) Isometric view. (b) Spanwise view. (c) Blade surface mesh.

4.0 Single-Passage Model

The procedure used for analyzing the TCT rotor was first performed on a single-passage model to verify the results before running a full-annulus case. The boundary conditions used for the single passage were radial profiles of total conditions and flow angles at inlet; mass flow exit; no slip wall for the blade, hub, and casing surfaces; and a periodic boundary condition for the connecting walls of the passage. Figure 3 shows the mesh used for the TCT configuration; fan rotation is around the x-axis and the primary flow is in the direction of positive x.

4.1 Steady Analysis

Figure 4 shows the TCT inlet profile used in the simulation with plots of inlet total pressure (Figure 4(a)), total temperature (Figure 4(b)), tangential flow angle (Figure 4(c)), and radial flow angle (Figure 4(d)). The inlet profile was taken as a circumferential average of the rotor inlet plane from a simulation that ran the TCT rotor with inlet and exit guide vanes, and an inflow distortion due to BLI.

A steady analysis for the single passage was performed to verify the design condition with a performance map and to create an initial case for the flutter analysis to follow. The performance map can be seen in Figure 5. At the design rotational speed, the physical mass flow rate varies between

approximately 7.5 and 10.2 kg/s, with the peak efficiency and design condition being approximately 9.5 kg/s. The vibration analysis for the single-passage case was run at the design condition.

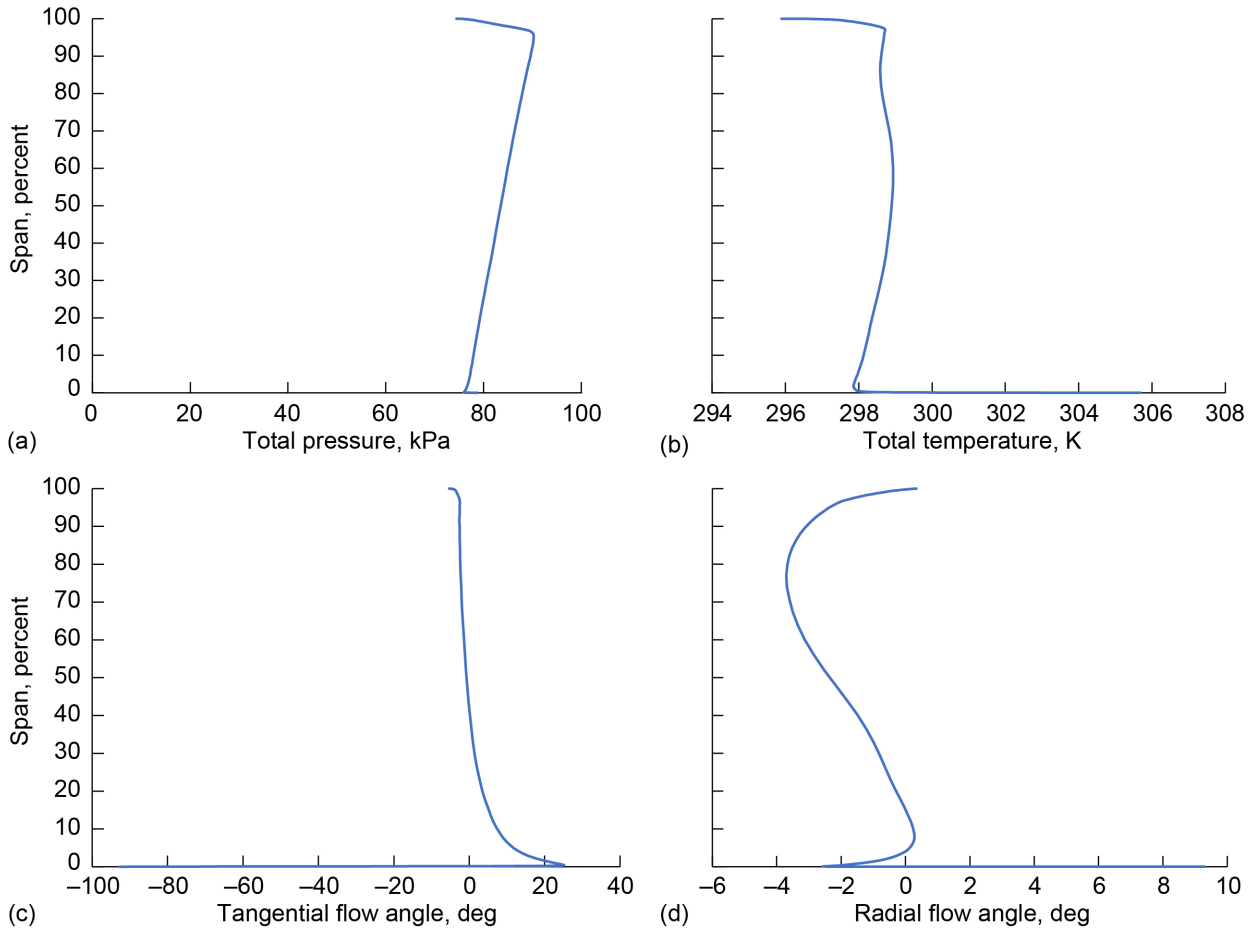

Figure 4.—TCT inlet profile. (a) Total pressure. (b) Total temperature. (c) Tangential flow angle. (d) Radial flow angle.

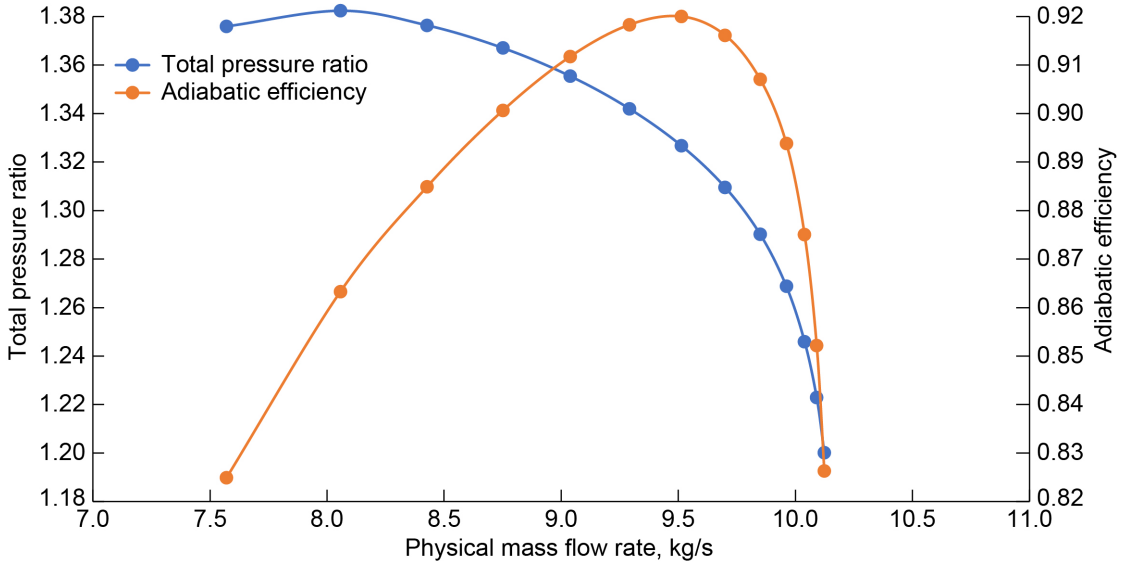

Figure 5.—TCT single-passage performance map.

4.2 Vibration and Flutter Analysis

The vibration analysis cases were run using the 8ND mode shapes for the first three modes. Grid deformation input files for TURBO were generated for all three modes using the approach described earlier. Various amplitudes were run for each mode to verify that the vibrational amplitudes were in the linear region and to find the maximum amplitude that can be run so that the impact of unsteady forces unrelated to the vibration are negligible when computing the work per cycle. Amplitudes that were too large caused the CFD code to give errors; for amplitudes that were too small, the unsteadiness of the flow dominated the vibrational effects, making them difficult to isolate. Each case was run for 10 vibration cycles to allow the work per cycle to converge for the passage. The largest scaling factors that successfully ran were 5×10^{-4}, 1×10^{-3}, and 1×10^{-4} for modes 1, 2, and 3, respectively. Figure 6 to Figure 8 show the convergence of (nondimensional) work per cycle for the three vibration modes at the largest amplitudes run. The reference quantity used in the nondimensionalization is the product of the specific heat ratio, the reference pressure, and a reference length to the third power. Table I to Table III summarize the various amplitudes run for the three vibrational modes as well as their converged work per cycle and corresponding aerodamping values. It is readily observed that the aerodamping results show very little variation with amplitude of vibration in the range of values prescribed in this study. The work per cycle has a quadratic dependence on the vibration amplitude due to the linear dependence of unsteady pressure on the amplitude and the use of scaled modal displacements, rather than the original unscaled modal displacements, in the work-per-cycle calculation.

Two short studies were performed for mode 1 using the 5×10^{-4} amplitude. The first study examined the sensitivity of the aerodamping with respect to the time step used. TURBO computes the time step based on the vibrational frequency and the time steps per period (vibration cycle). Figure 9 plots the converged aerodamping value against the time steps per period. The computed aerodamping appears to stabilize after around 140 time steps per period. It can be observed that the variation in the aerodamping is very small throughout the range of time steps in this study. The single-passage cases were run using 120 time steps per period. There was no need to rerun these cases because the variation with respect to the time step was negligible.

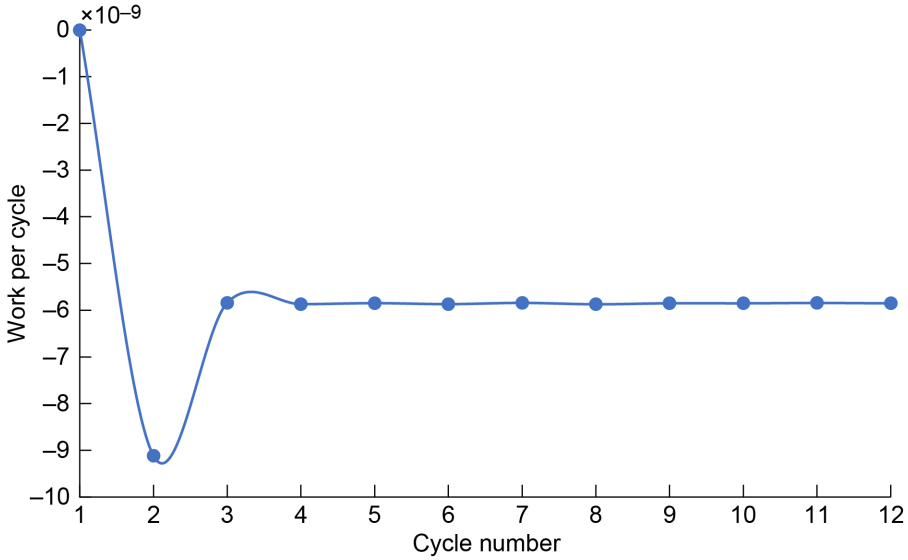

Figure 6.—TCT single-passage mode 1 work per cycle.

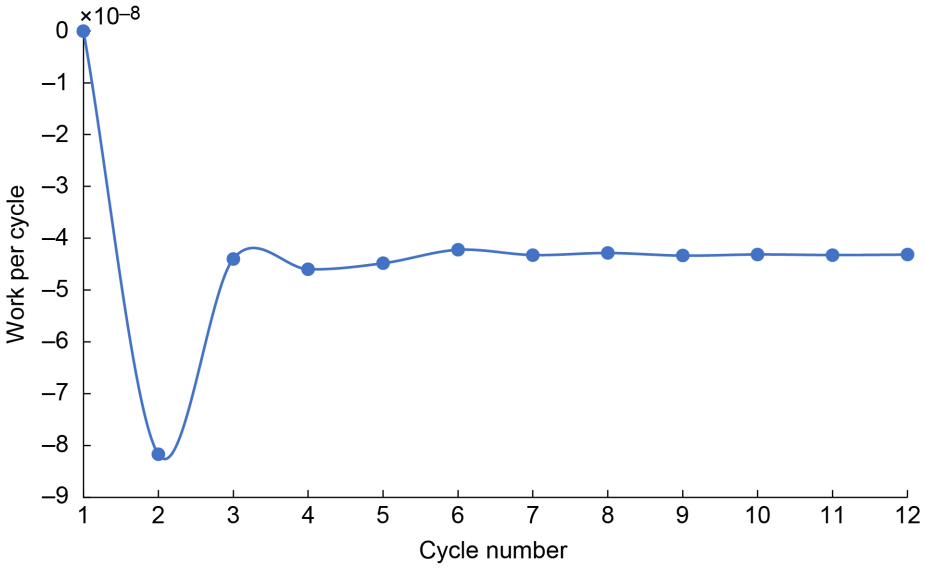

Figure 7.—TCT single-passage mode 2 work per cycle.

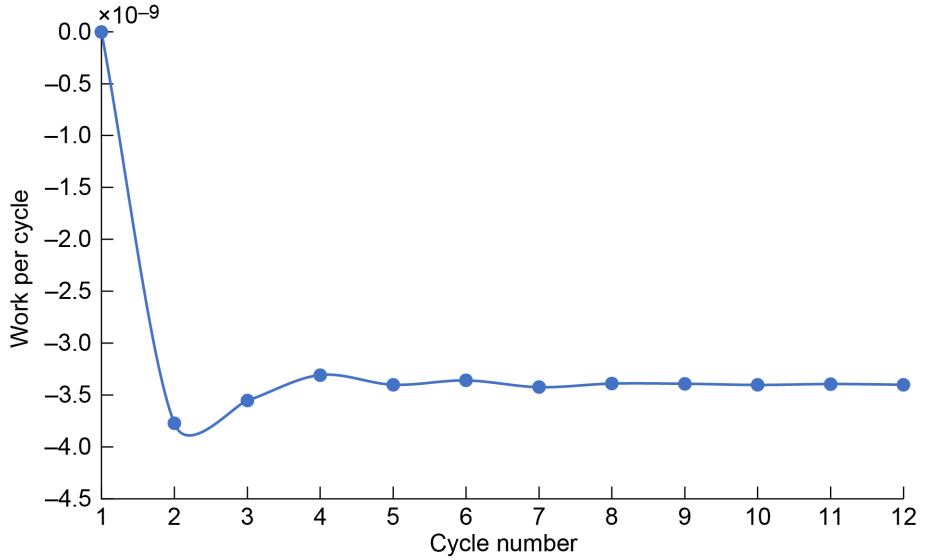

Figure 8.—TCT single-passage mode 3 work per cycle.

TABLE I.—TCT SINGLE-PASSAGE MODE 1 AERODAMPING

Amplitude	Work per cycle	Aerodamping, percent
1×10^{-5}	-2.39×10^{-12}	0.273
5×10^{-5}	-5.90×10^{-11}	0.270
1×10^{-4}	-2.34×10^{-10}	0.268
5×10^{-4}	-5.85×10^{-9}	0.268

TABLE II.—TCT SINGLE-PASSAGE MODE 2 AERODAMPING

Amplitude	Work per cycle	Aerodamping, percent
1×10^{-5}	-4.34×10^{-12}	0.0797
5×10^{-5}	-1.08×10^{-10}	0.0794
1×10^{-4}	-4.32×10^{-10}	0.0793
5×10^{-4}	-1.08×10^{-8}	0.0792
1×10^{-3}	-4.32×10^{-8}	0.0792

TABLE III.—TCT SINGLE-PASSAGE MODE 3 AERODAMPING

Amplitude	Work per cycle	Aerodamping, percent
1×10^{-5}	-3.39×10^{-11}	0.520
5×10^{-5}	-8.48×10^{-10}	0.520
1×10^{-4}	-3.40×10^{-9}	0.522

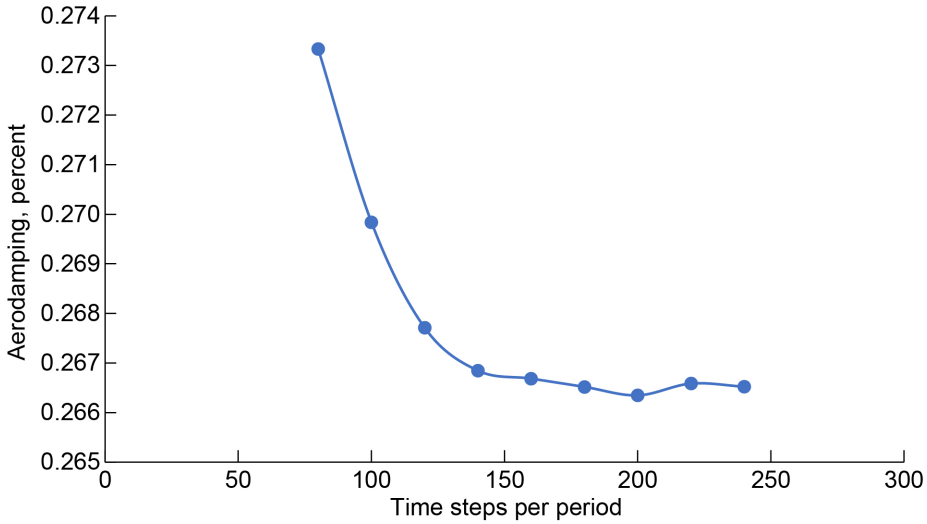

Figure 9.—TCT single-passage mode 1 time-step sensitivity.

The second study examined the sensitivity of the aerodamping with respect to the decay coefficient used in the exponential decay function applied to the deformation propagation from the blade surface to the interior passage mesh. The decay coefficient was varied between 1 and 18 for both cases; the higher values of decay coefficient correspond to a more rapid dropoff of the mesh deformation near the blade surface. Figure 2 shows the propagation of the deformations at a constant radial cross section for the decay coefficient of 1. Figure 10 shows the deformation propagation contours for decay coefficients of 9 and 18, respectively. For decay coefficient values of 20 or higher, the aerodamping values did not converge. Figure 11 shows the plot of the decay coefficient values versus the aerodamping for mode 1; a linear trend is clearly seen between the aerodamping and the decay coefficient. A similar study was performed on the fan configuration analyzed in previous work (Refs. 4 and 5), which also showed a similar trend between the aerodamping and the decay coefficient. These results are plotted in Figure 12. The similar results between the two cases suggest that the observed sensitivity is not dependent on the particular geometry or the mesh characteristics.

The decay coefficient sensitivity study for the TCT geometry was expanded to include negative values for the decay coefficient. Negative decay coefficients also result in a decrease in the mesh deformation approaching the mesh bounds; however, the rate of decay is significantly lower near the blade and higher near the boundary as the decay coefficient decreases. Figure 13 shows the deformation contours for decay coefficients of –1 and –4, respectively, showing the deformation values remaining high in the interior of the passage before dropping off rapidly near the outer boundary. The effect of the negative decay coefficients on the aerodamping still appears linear; however, a transition in the slope of the relation appears to occur as the decay coefficient approaches 0. The resulting slope in the negative region appears to be significantly smaller in magnitude than in the positive region, suggesting that negative decay coefficients have a weaker effect on the aerodamping. This trend can be observed in Figure 14.

Further work is needed to understand the dependence of aerodamping on the decay coefficient. Analyses of the contributions to the work from different parts of the blade surface may provide some guidance in determining regions of the mesh and unsteady flow that need closer examination. Another researcher is investigating the possibility that the turbulence wall model is affecting the unsteady flow near the blade and the resulting unsteady pressure on the blade. The objective is to obtain results that are independent of, or at the least not overly sensitive to, the details of the deformation in the passage (for the same blade surface deformations). In most of the remainder of the current study, a decay coefficient of 1 was used, as it resulted in grid deformations that appear reasonable without large gradients near the blade or the passage boundary. Figure 15 and Figure 16 present a visual summary of the deformation functions and contour plots of deformations within the passage. Also, the resulting aerodamping for this decay coefficient falls within a region of small variation. A sensitivity study was also performed to determine the effect of the decay coefficient on the aerodamping for the full-annulus analyses for various nodal diameters.

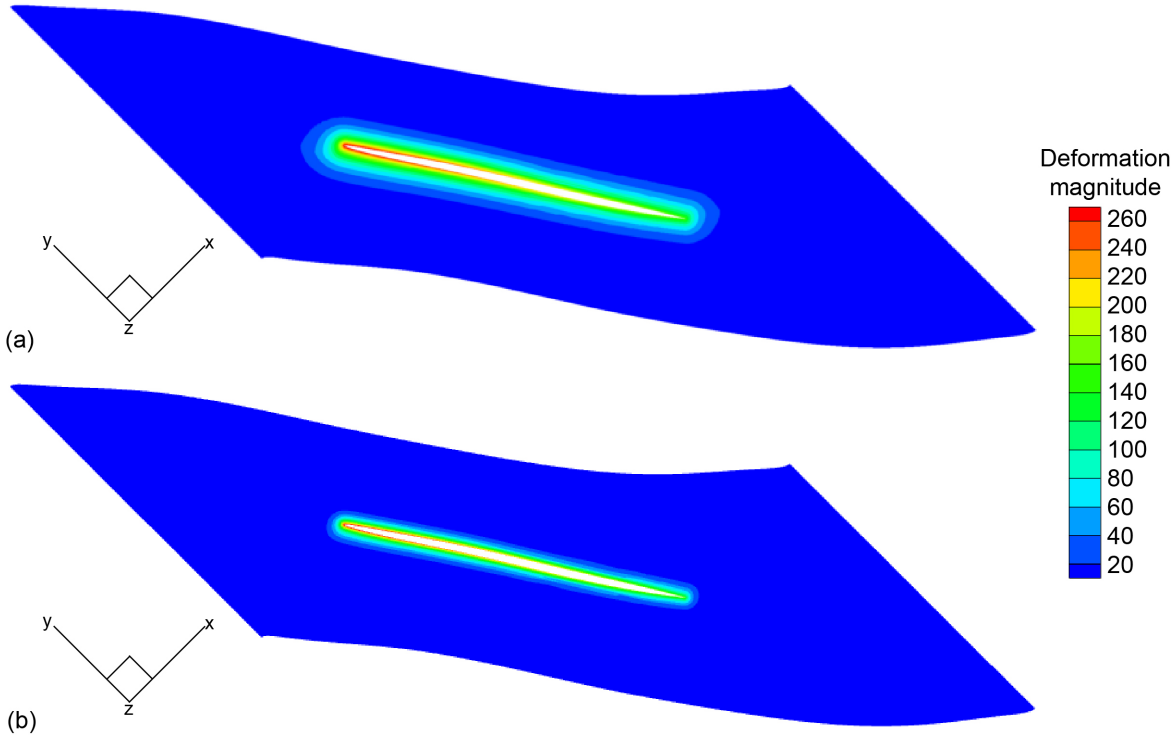

Figure 10.—TCT mode 1 deformation propagation at constant radius. (a) Decay coefficient = 9. (b) Decay coefficient = 18.

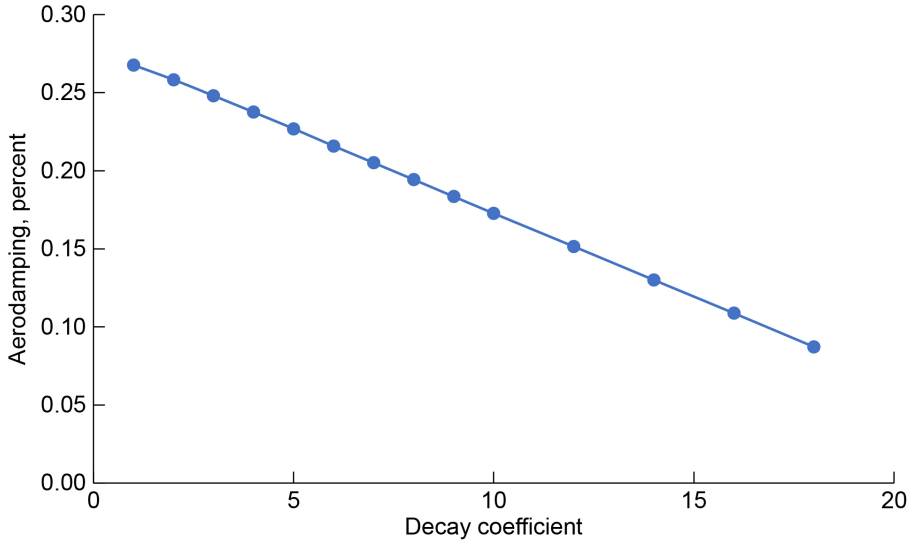

Figure 11.—TCT single-passage mode 1 decay coefficient sensitivity.

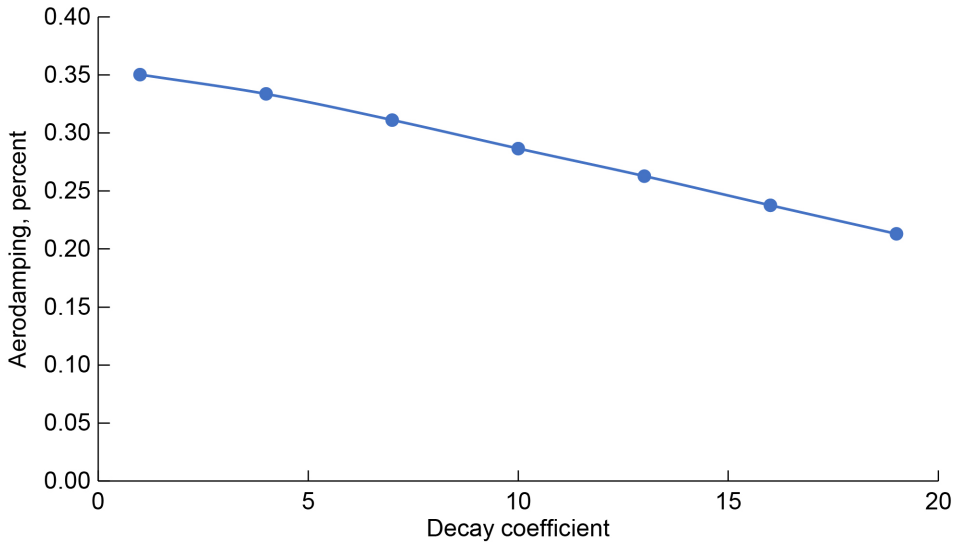

Figure 12.—Decay coefficient sensitivity for distortion-tolerant fan.

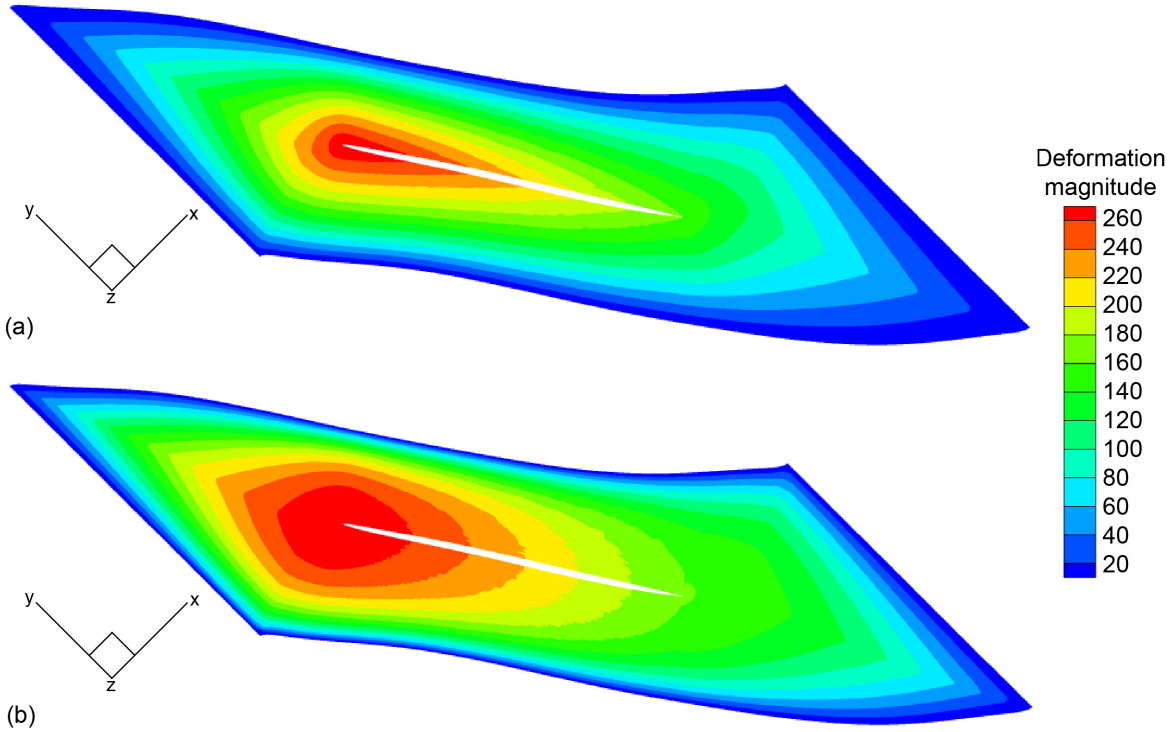

Figure 13.—TCT mode 1 deformation propagation at constant radius. (a) Decay coefficient = –1. (b) Decay coefficient = –4.

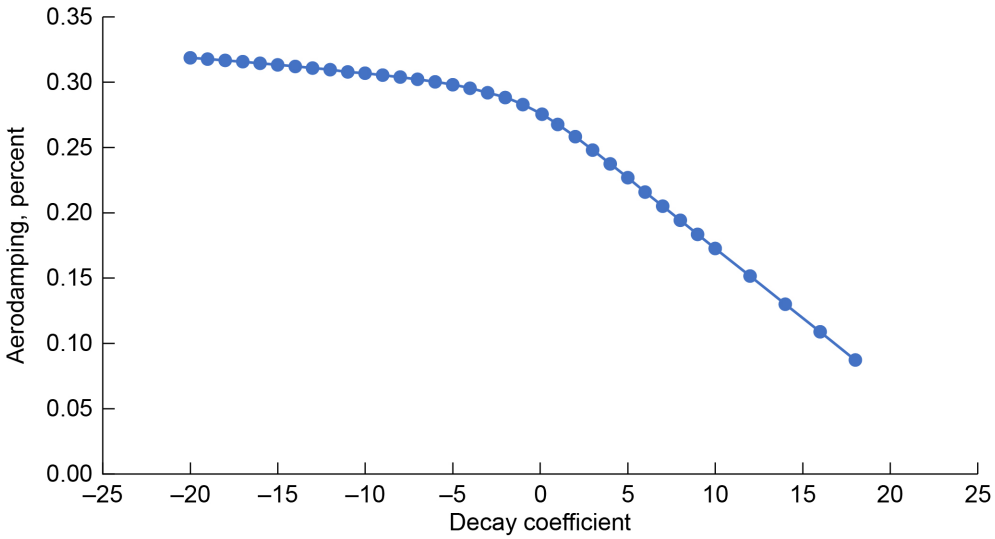

Figure 14.—TCT single-passage mode 1 decay coefficient sensitivity over extended range.

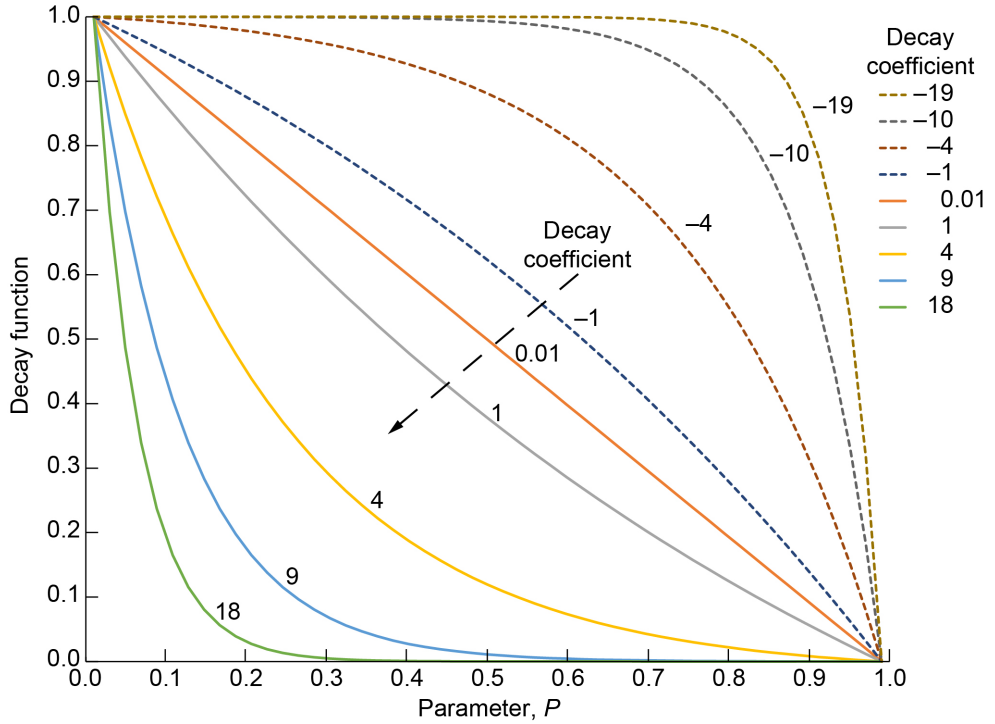

Figure 15.—Visualization of decay of displacements from blade surface (P = 0.0) to boundary (P = 1.0) for various values of decay coefficient considered, including baseline value of 1.

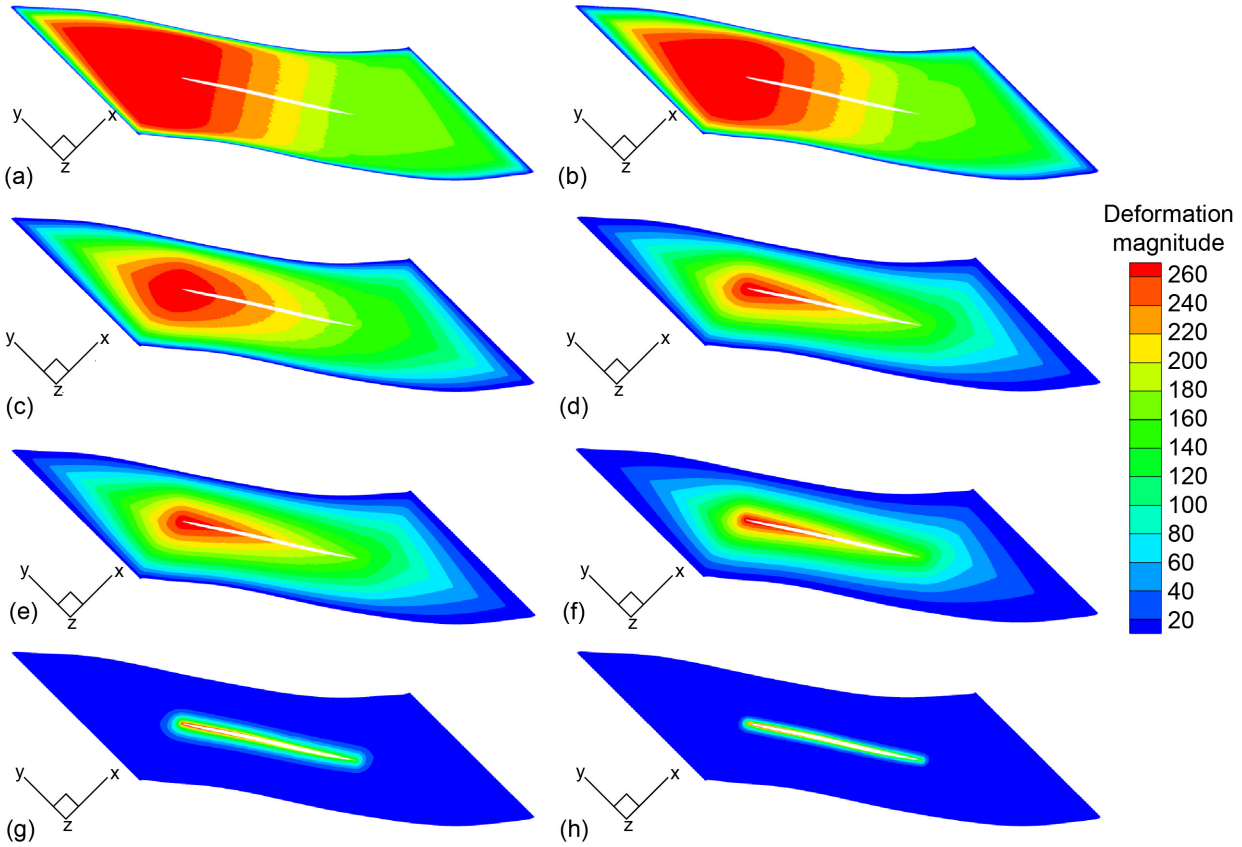

Figure 16.—Contours of in-passage deformation for various values of decay coefficient λ computed via exponential decay function defined in Equation (2). (a) λ = –19. (b) λ = –10. (c) λ = –4. (d) λ = –1. (e) λ = 1 (baseline value). (f) λ = 4. (g) λ = 9. (h) λ = 18.

5.0 Full-Annulus Model

The full-annulus analysis was started with a steady run that was used to provide initial results for the blade vibration analyses. Vibrational analysis was first performed at the design condition for in-phase blade vibrations without any phasing between the blade passages. Later, the deformation propagation code was modified to include a constant interblade phase angle between adjacent blades (and blade passages) to model the different nodal diameters. Analyses with blade vibrations were performed for the TCT geometry using TURBO for all possible nodal diameters at the design condition and at the near-stall condition. The boundary conditions used for each case included mass flow rate at exit, radial profiles of total conditions and flow angles at inlet, and no-slip walls for the hub, casing, and blades.

5.1 Steady Run

The steady run was initialized using results from another ongoing study, which includes inlet and exit guide vanes in addition to the TCT rotor and an inflow BLI distortion. The inflow profile and the initial flow field for the present TCT full-annulus case were derived from the TCT stage of that study. The converged steady-run results were then used as an initial condition for a mass flow sweep to produce a performance map, shown in Figure 17. The single-passage performance map is also included in Figure 17 for comparison. Each steady analysis used the nearest converged solution as an initial solution to accelerate convergence.

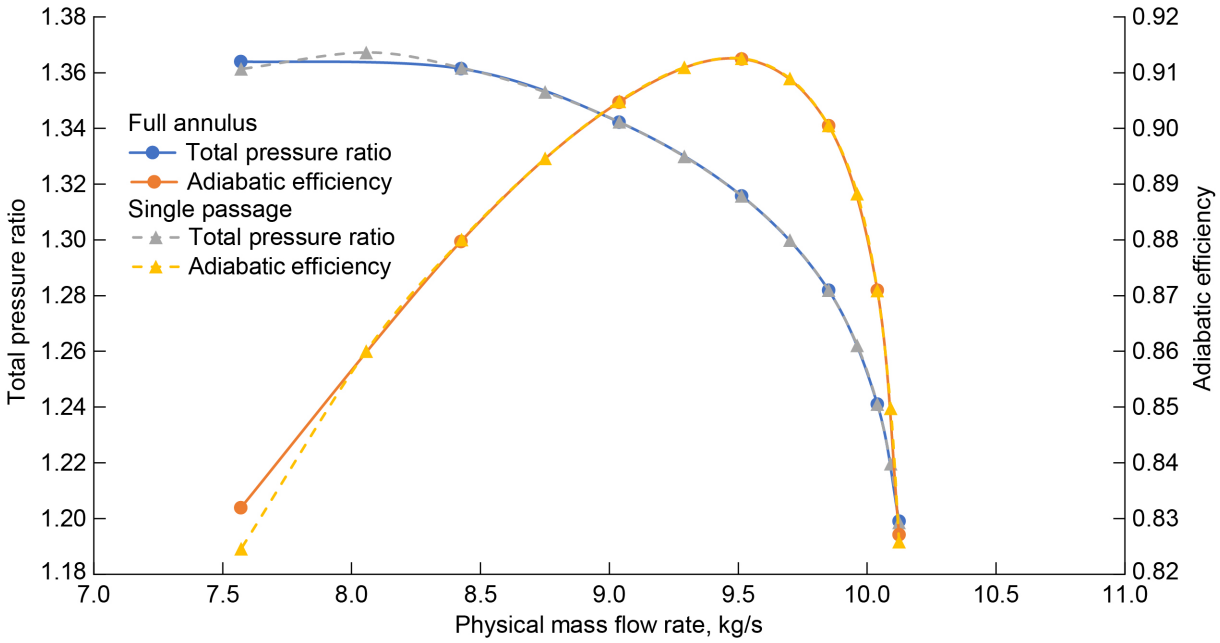

Figure 17.—TCT single-passage and full-annulus performance maps.

5.2 Vibration and Flutter Analysis at Design Condition

For the full-annulus models, most of the analyses used deformations with a decay coefficient of 1. A sensitivity study of decay coefficient was also performed. Mode 1 cases were run with 140 time steps per period, and modes 2 and 3 cases were run with 120 time steps per period. Cases with 0 phase, 0ND, were initially run to compare with the single-passage results. The converged results of the 0ND cases for modes 1 to 3 are plotted against the corresponding cases from the single passage in Figure 18 to Figure 20. The averaged work per cycle from full-annulus analyses differs from corresponding single-passage results by about 1.5, 0.6, and 2.9 percent for modes 1, 2, and 3, respectively.

Cases were run using a phase-angle of 180°/8ND and 90°/4ND to test the phasing capabilities of the code used for the deformation file generation. The work-per-cycle convergence plotted against the cycle number for the three modes with the 8ND phases is shown in Figure 21 to Figure 23. Figure 24 and Figure 25 show the time history of cumulative work from the beginning of each vibration cycle for adjacent passages (adjacent blades) for the mode 1 8ND and 4ND cases (respectively) to validate that the phasing was implemented correctly. The two passages plotted in Figure 24 are each 180° out of phase with respect to each other, whereas the four passages plotted in Figure 25 are 90° out of phase. Note that in Figure 25 the blades in each passage are at different positions at the start of the vibration, with two blades being at zero displacement and two blades being at the minimum and maximum displacement due to the 90° phase between adjacent blades (and passages). These differences are then reflected in the cumulative work history plot showing a different range of values for adjacent blades.

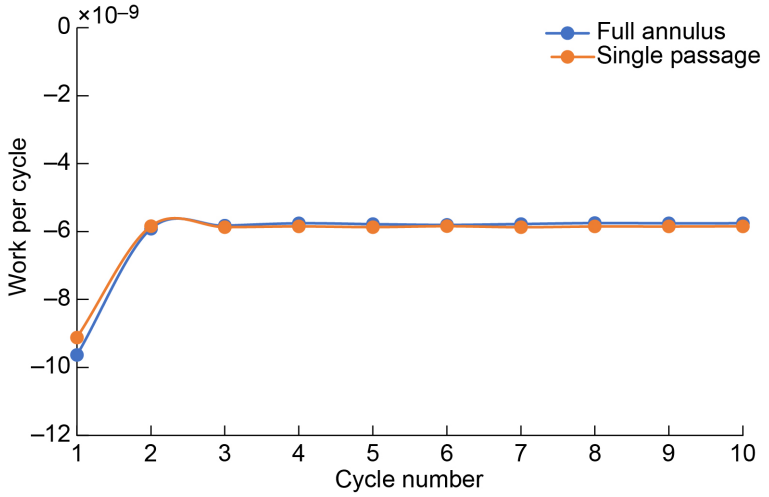

Figure 18.—TCT single-passage and full-annulus mode 1 0ND work per cycle.

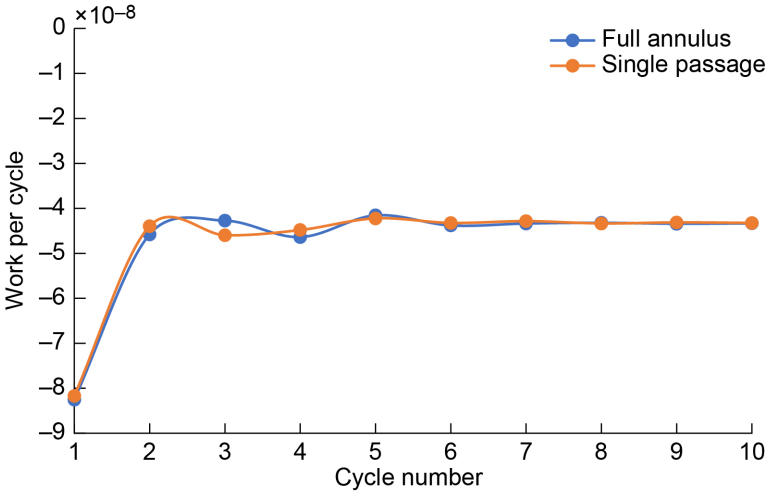

Figure 19.—TCT single-passage and full-annulus mode 2 0ND work per cycle.

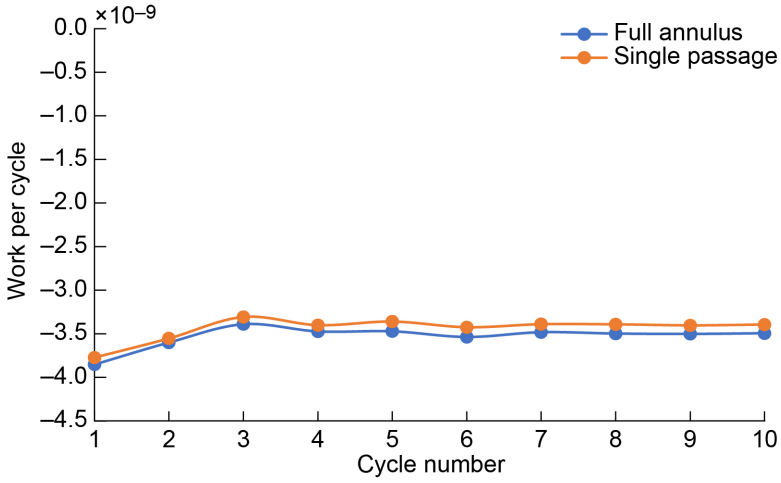

Figure 20.—TCT single-passage and full-annulus mode 3 0ND work per cycle.

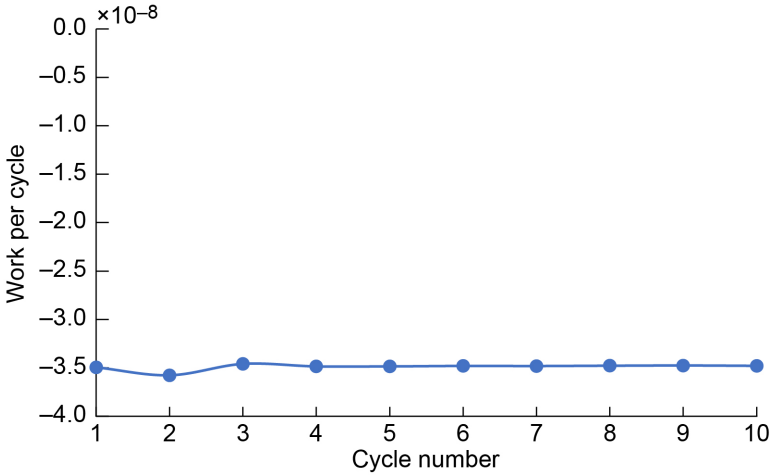

Figure 21.—TCT full-annulus mode 1 8ND work per cycle.

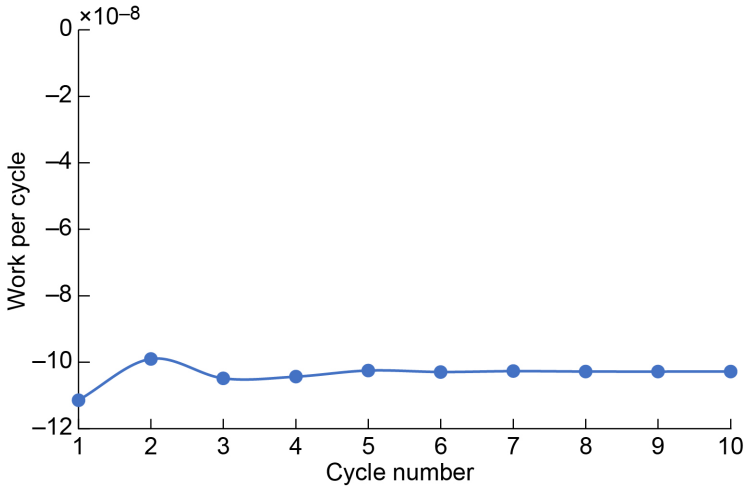

Figure 22.—TCT full-annulus mode 2 8ND work per cycle.

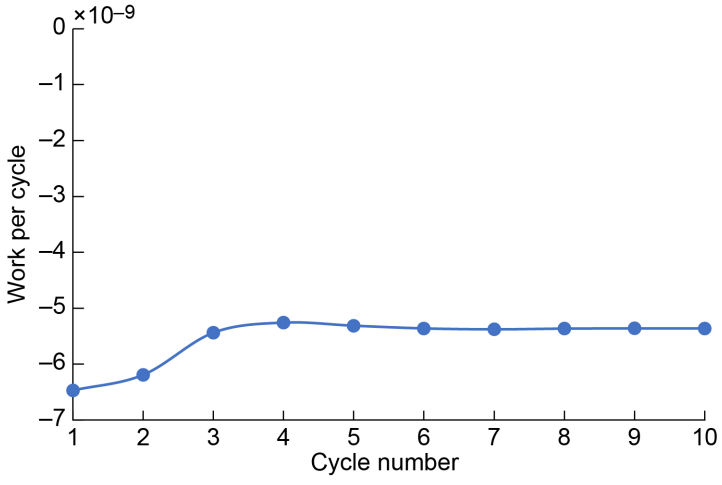

Figure 23.—TCT full-annulus mode 3 8ND work per cycle.

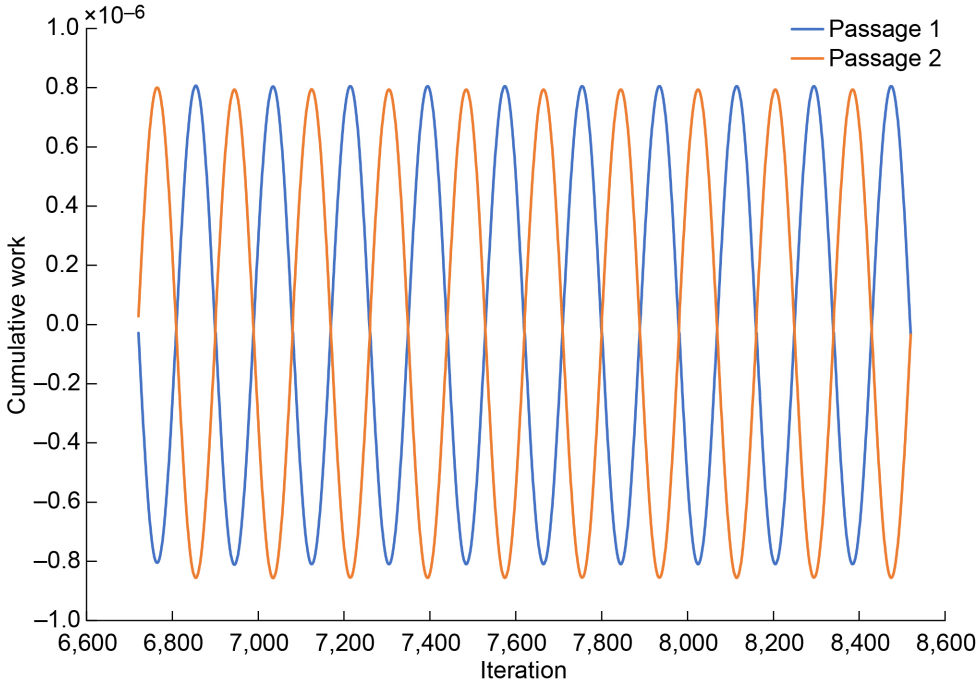

Figure 24.—TCT full-annulus mode 1 8ND work history for two adjacent passages.

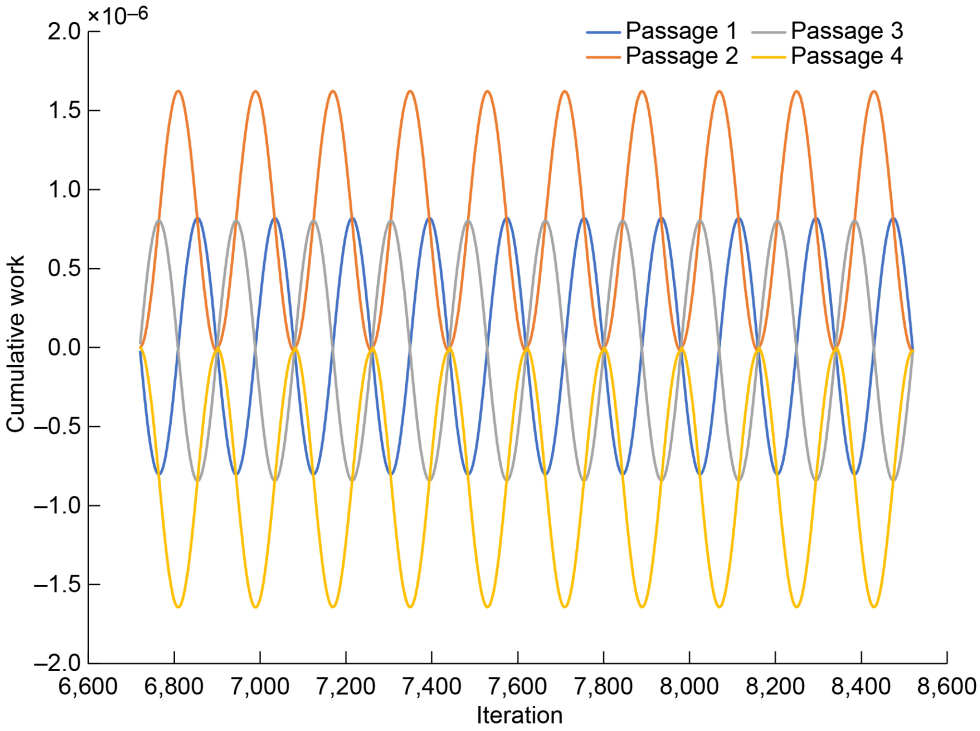

Figure 25.—TCT full-annulus mode 1 4ND work history for four adjacent passages.

Cases for the other possible nodal diameters were run for all three modes, yielding 48 cases in total with 16 nodal diameter configurations per mode. Due to the large number of cases run, the setup and analysis were automated using a separate Fortran code that also extracted key results for each case after analysis was complete. The nearly converged values of work per cycle for each case were averaged over all blades and over several cycles to obtain the computed work per cycle for the given case. Standard deviations were computed to verify the convergence of the aerodamping. Table IV tabulates all of the results, and Figure 26 plots the aerodamping values against the nodal diameters.

The aerodamping values for each case shown in Table IV and Figure 26 are positive, but some values are close to zero. The positive value of the aerodamping indicates that blade vibrations would decay. As a result, based on these analyses at design conditions, the TCT fan rotor would not be expected to encounter flutter or structural failure due to the aeroelastic instability. The low values of aerodamping for mode 2 are of concern, as this rotor would have very low material damping and no mechanical damping due to the integrally bladed (blisk) rotor design.

TABLE IV.—TCT FULL-ANNULUS AERODAMPING RESULTS AT DESIGN CONDITION

Mode 1			Mode 2			Mode 3		
ND	Aerodamping, %	Standard deviation, %	ND	Aerodamping, %	Standard deviation, %	ND	Aerodamping, %	Standard deviation, %
8	1.59	0.001	8	0.19	0.000	8	0.82	0.003
7	1.54	0.004	7	0.17	0.000	7	0.76	0.001
6	1.44	0.003	6	0.16	0.000	6	0.73	0.001
5	1.27	0.004	5	0.15	0.001	5	0.71	0.001
4	0.95	0.003	4	0.14	0.001	4	0.68	0.002
3	0.51	0.002	3	0.12	0.000	3	0.66	0.003
2	0.22	0.001	2	0.09	0.001	2	0.62	0.003
1	0.19	0.001	1	0.08	0.001	1	0.58	0.002
0	0.26	0.001	0	0.08	0.001	0	0.54	0.003
–1	0.49	0.001	–1	0.10	0.001	–1	0.51	0.003
–2	0.82	0.000	–2	0.14	0.001	–2	0.57	0.003
–3	1.10	0.000	–3	0.19	0.001	–3	0.87	0.002
–4	1.27	0.001	–4	0.21	0.001	–4	1.10	0.004
–5	1.41	0.001	–5	0.22	0.000	–5	1.07	0.006
–6	1.52	0.001	–6	0.21	0.000	–6	1.00	0.004
–7	1.59	0.001	–7	0.20	0.000	–7	0.91	0.003
–8	1.59	0.001	–8	0.19	0.000	–8	0.82	0.003

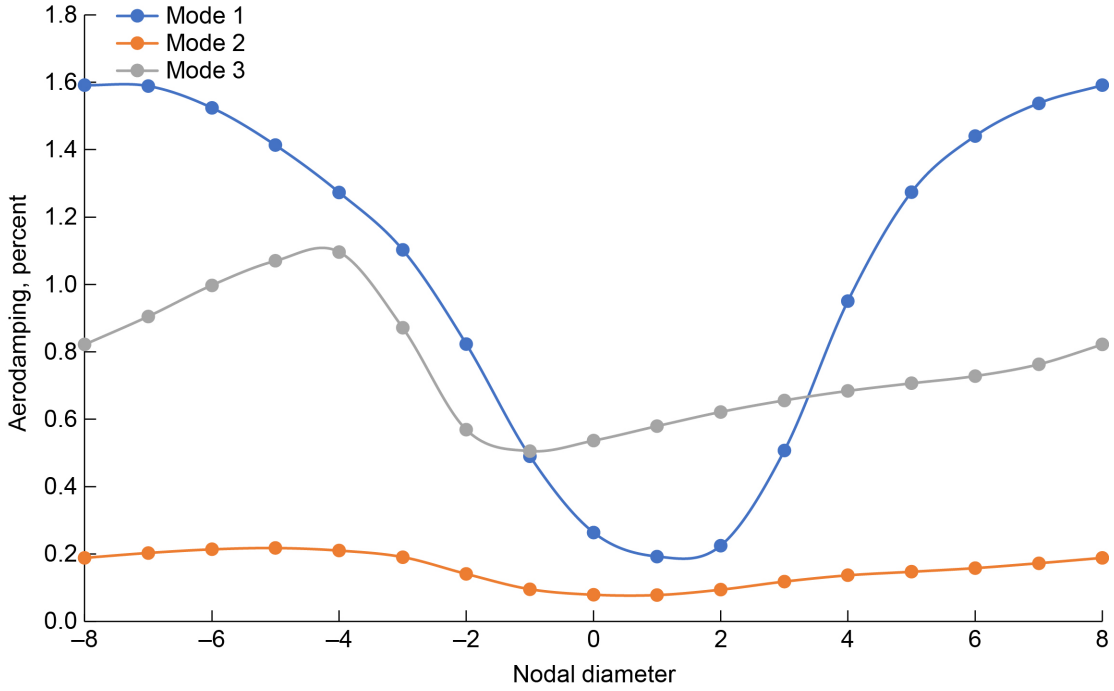

Figure 26.—TCT full-annulus aerodamping variation with nodal diameter at design condition.

5.3 Vibration and Flutter Analysis at Near-Stall Conditions

The same analysis performed for the design condition point was also performed for the near-stall condition, which corresponds to a physical mass flow rate of about 7.5 kg/s. Results for all possible nodal diameters for the three modes are summarized in Table V and Figure 27. Unlike the results at design condition, the aerodamping is predicted to drop below zero for the 1ND, 2ND, and 3ND cases of mode 1, which indicates an increase in blade vibrations due to the aerodynamic effects, suggesting that flutter may occur for these three nodal diameters of mode 1, with 2ND being the most unstable.

A third operating condition was then analyzed just above the stall condition at a physical mass flow rate of approximately 8 kg/s. The results of this study are summarized in Table VI and Figure 28. The aerodamping for mode 1 at this above-stall condition does remain positive for all nodal diameters, but the values are nearly zero for 1ND and 2ND, indicating the onset of flutter at or near this flow condition.

TABLE V.—TCT FULL-ANNULUS AERODAMPING RESULTS AT NEAR-STALL CONDITION

Mode 1			Mode 2			Mode 3		
ND	Aerodamping, %	Standard deviation, %	ND	Aerodamping, %	Standard deviation, %	ND	Aerodamping, %	Standard deviation, %
8	2.86	0.033	8	0.26	0.004	8	0.75	0.027
7	3.69	0.032	7	0.23	0.001	7	0.74	0.039
6	3.89	0.021	6	0.21	0.001	6	0.69	0.029
5	2.50	0.045	5	0.18	0.002	5	0.70	0.046
4	0.68	0.022	4	0.15	0.001	4	0.79	0.034
3	–0.08	0.014	3	0.13	0.001	3	1.06	0.025
2	–0.23	0.012	2	0.11	0.001	2	1.25	0.022
1	–0.21	0.032	1	0.10	0.001	1	1.26	0.035
0	0.19	0.010	0	0.30	0.004	0	0.84	0.090
–1	0.16	0.037	–1	0.12	0.000	–1	1.01	0.049
–2	0.45	0.016	–2	0.15	0.002	–2	1.10	0.037
–3	0.55	0.012	–3	0.18	0.001	–3	1.29	0.045
–4	0.72	0.015	–4	0.21	0.002	–4	1.11	0.026
–5	1.00	0.022	–5	0.23	0.001	–5	0.71	0.039
–6	1.42	0.026	–6	0.25	0.002	–6	0.69	0.013
–7	2.00	0.021	–7	0.25	0.001	–7	0.71	0.033
–8	2.86	0.033	–8	0.26	0.004	–8	0.75	0.027

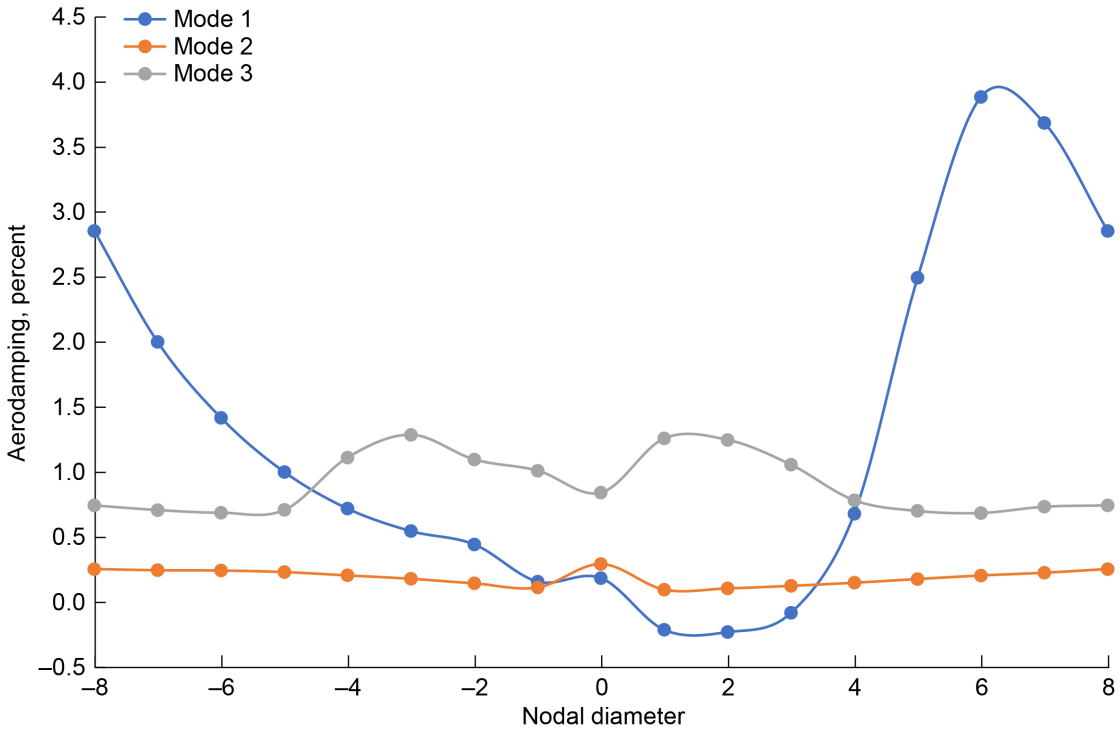

Figure 27.—TCT full-annulus nodal diameter versus aerodamping at near-stall condition.

TABLE VI.—TCT FULL-ANNULUS AERODAMPING RESULTS AT ABOVE-STALL CONDITION

Mode 1			Mode 2			Mode 3		
ND	Aerodamping, %	Standard deviation, %	ND	Aerodamping, %	Standard deviation, %	ND	Aerodamping, %	Standard deviation, %
8	2.91	0.006	8	0.28	0.001	8	0.71	0.002
7	3.06	0.011	7	0.23	0.009	7	0.77	0.003
6	2.46	0.008	6	0.22	0.007	6	0.83	0.005
5	1.52	0.010	5	0.19	0.009	5	0.90	0.005
4	0.72	0.014	4	0.16	0.003	4	0.95	0.003
3	0.23	0.003	3	0.13	0.004	3	0.98	0.002
2	0.01	0.003	2	0.11	0.002	2	0.97	0.001
1	0.00	0.003	1	0.10	0.002	1	0.93	0.005
0	0.21	0.003	0	0.09	0.001	0	0.65	0.003
–1	0.29	0.001	–1	0.12	0.004	–1	0.74	0.005
–2	0.60	0.001	–2	0.16	0.005	–2	0.68	0.016
–3	0.80	0.002	–3	0.18	0.003	–3	0.76	0.006
–4	1.04	0.006	–4	0.22	0.001	–4	0.71	0.006
–5	1.37	0.006	–5	0.23	0.001	–5	0.60	0.001
–6	1.81	0.013	–6	0.25	0.005	–6	0.63	0.001
–7	2.35	0.006	–7	0.25	0.006	–7	0.67	0.002
–8	2.91	0.006	–8	0.28	0.001	–8	0.71	0.002

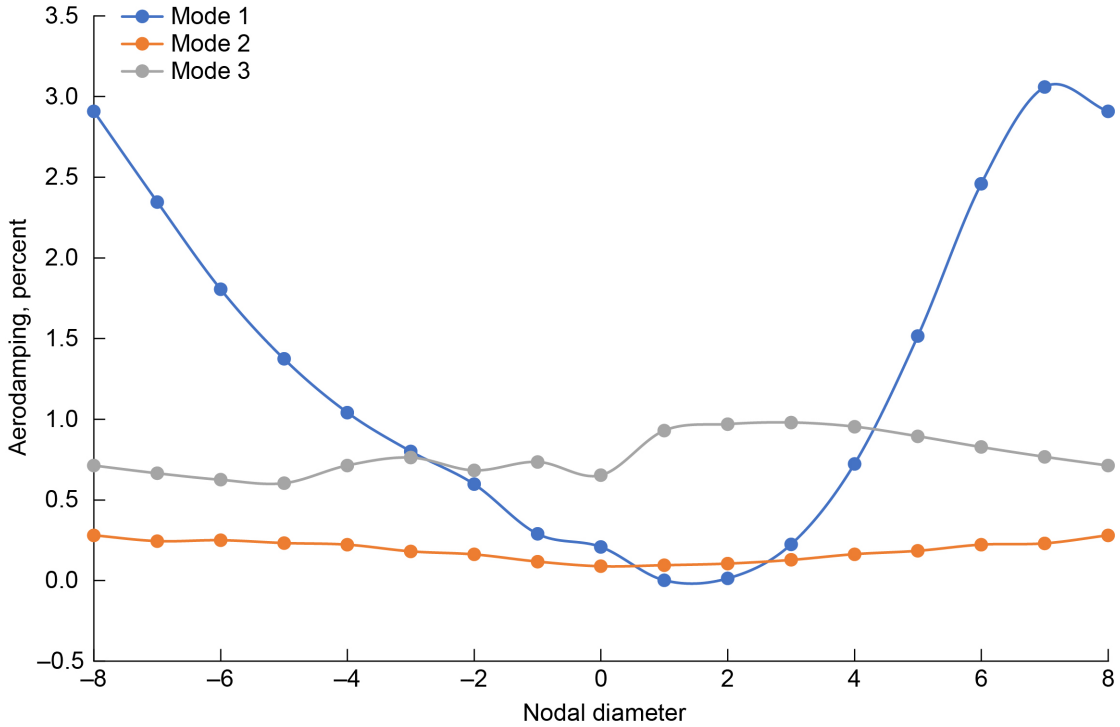

Figure 28.—TCT full-annulus nodal diameter versus aerodamping at an above-stall condition.

5.4 Full-Annulus Decay Coefficient Sensitivity Study

A decay coefficient sensitivity study was performed for the full annulus at the near-stall condition at select nodal diameters to verify if varying the decay coefficient would result in a change in the sign of the predicted aerodamping value. Results can be seen in Figure 29. The study was performed on –4ND, –1ND, 0ND, 2ND, 4ND, and 8ND cases with decay coefficients varying from 1 to 19 in increments of three. The aerodamping of the 2ND case remained negative, whereas the predicted aerodamping for the –4ND, 4ND, and 8ND cases remained positive for all tested decay coefficients. The –4ND case with a decay coefficient of 19 did not converge. The predicted aerodamping for the –1ND and 0ND cases switched from a positive to a negative value as the decay coefficient increased.

The rate of change of the predicted aerodamping versus the decay coefficient varied depending on the nodal diameter. Notably, the 8ND case showed an increase in the aerodamping as the decay coefficient increased. It can also be observed from Figure 29 that the –4ND case shows an approximately constant aerodamping for the range of decay coefficient. Note that the nodal diameters correspond to a phase angle in blade-surface deformations between passages. For the TCT case, 8ND and –8ND correspond to 180 and –180°, respectively. Thus, the 8ND and –8ND cases should have identical values. The cyclical nature of the phase angle, and therefore the nodal diameter, suggests that at some point between –180 and 180°, a transition occurs around the –4ND case where the relation between the aerodamping and decay coefficient changes from a negative slope to a positive slope. A similar conclusion can be made for a point between the 4ND and 8ND cases. Cases in which the aerodamping increases with respect to the decay coefficient should remain outside the risk of flutter. Therefore, the cases that are at risk are the nodal diameters between and including –3 and 4. This assumes that the trends are similar for modes 2 and 3. Tests will need to be performed on the 5ND and 6ND cases to verify where the change in the relationship occurs.

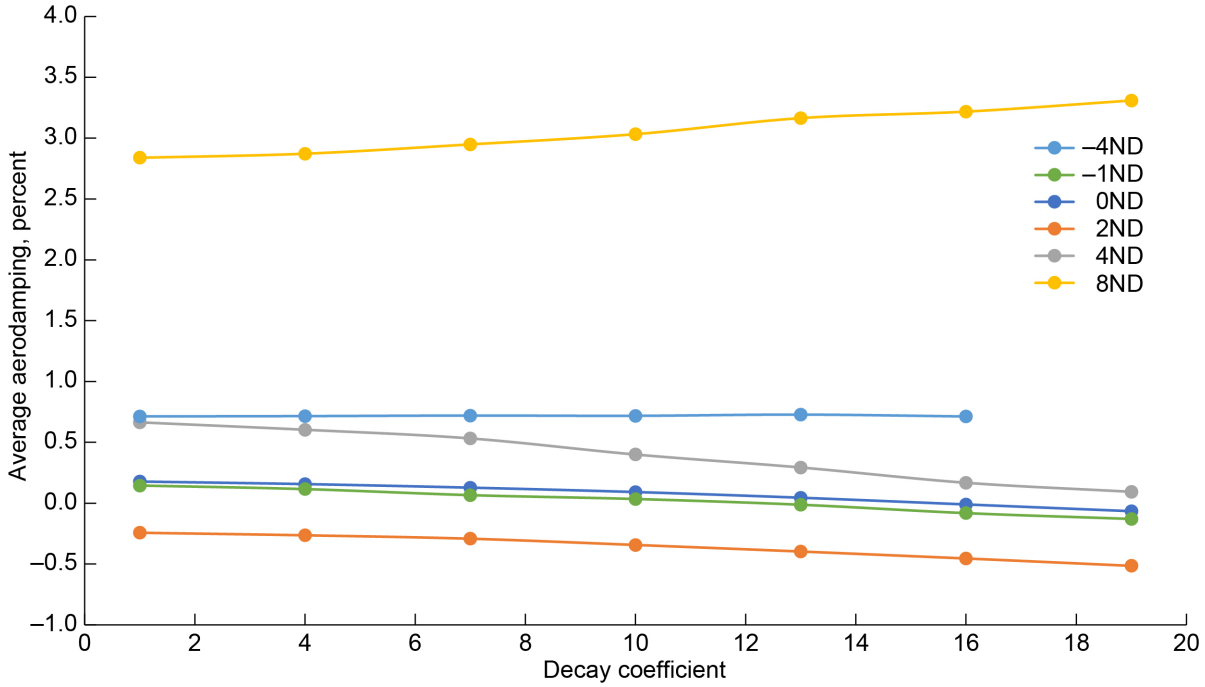

Figure 29.—TCT full-annulus mode 1 decay coefficient sensitivity.

6.0 Conclusion

Computational fluid dynamics (CFD) analysis with an unsteady Reynolds-averaged Navier–Stokes solver was used to predict the potential for fan blade flutter to occur for the tail-cone thruster (TCT) geometry. Prescribed blade vibrations, based on mode shapes from finite element analyses, were used to calculate the work per cycle and aerodynamic damping (aerodamping) based on the energy method. A new algorithm was developed and used to propagate the grid deformations from the blade surface into the interior of the passage to the passage boundary. This algorithm uses an exponential decay function for the mesh deformation in the interior of the passage. Phasing of deformations between passages is also incorporated to simulate traveling wave vibrations. Sensitivity studies performed for analyses of a single blade passage showed a highly linear dependence of calculated aerodamping on the decay coefficient used in the propagation of the deformations. Initial investigations into these results suggest this dependence could be a result of the way the CFD modeling handles large mesh changes due to blade vibrations, particularly near the tip of the blade, where the mesh deformations are largest. Additional work performed by another researcher points to the turbulence wall model as a possible factor. Further work is needed to identify the primary cause of the dependence of aerodamping on grid deformation decay coefficient.

The results of the full-annulus studies predict the possibility of flutter in the first mode as the flow field approaches the stall condition. For three nodal diameter patterns at the near-stall condition, the aerodamping becomes negative, but for all other nodal diameters and for all modes examined, the aerodamping remains positive. It is important to keep in mind the observed sensitivity of the results to variations in the decay coefficient used in the propagation of the surface displacements throughout the mesh. The strong dependence of calculated aerodamping on the decay coefficient points clearly to a need for more analysis and investigation to understand the cause and determine the best way to obtain results that are not overly sensitive to this numerical parameter. More work is needed in understanding these sensitivities before any recommendations can be made to modify the design of the TCT geometry prior to experimental verification.

References

1. Ashcraft, Scott W., et al.: Review of Propulsion Technologies for N+3 Subsonic Vehicle Concepts. NASA/TM—2011-217239, 2011. https://ntrs.nasa.gov
2. Plas, Angelique: Performance of a Boundary Layer Ingesting Propulsion System. M.S. Thesis, Massachusetts Institute of Technology, 2006.
3. Smith, Leroy H., Jr.: Wake Ingestion Propulsion Benefit. J. Propuls. Power, vol. 9, no. 1, 1993.
4. Bakhle, Milind A.; Reddy, T.S.R.; and Coroneos, Rula M.: Forced Response Analysis of a Fan With Boundary Layer Inlet Distortion. AIAA 2014–3734, 2014.
5. Bakhle, Milind A., et al.: Aeromechanics Analysis of a Distortion-Tolerant Fan With Boundary Layer Ingestion. AIAA 2018–1891, 2018.
6. Carta, F.O.: Coupled Blade-Disk-Shroud Flutter Instabilities in Turbojet Engine Rotors. J. Eng. Power, vol. 89, no. 3, 1967, pp. 419–426.
7. Giuliani, James E.; and Chen, Jen-Ping: Fan Response to Boundary-Layer Ingesting Inlet Distortions. AIAA J., vol. 54, no. 10, 2016, pp. 3232–3243.

Appendix—Nomenclature

Acronyms

BLI	boundary-layer ingestion
CFD	computational fluid dynamics
FEM	finite element method
ND	nodal diameter
TCT	tail-cone thruster

Symbols

b	blade passage number
d	distance
k	turbulent kinetic energy
n	index associated with a point on the edge of the tip gap region
P	parameter value
p	point
$\Delta x,y,z$	deformation components
ε	turbulent kinetic energy dissipation rate
ζ	damping ratio expressed as percent of critical damping
θ	pitch angle
λ	decay coefficient
φ	interblade phase angle

Subscripts

$b = 1$	blade passage used to compute initial mesh deformations
bld	blade
bnd	bounds of the mesh
cas	value at the casing
edge	edge of tip gap region
i	imaginary
r	real